Research Square

Preprints are preliminary reports that have not undergone peer review.
They should not be considered conclusive, used to inform clinical practice,
or referenced by the media as validated information.

Neem-Mediated Morphology Evolution and Mg-Incorporated Cobalt Oxide Electrode Material for Supercapacitor Application

Pankaj G. Patil
Pratishthan Mahavidyalaya, Paithan 431107, Chatrapati Sambhajinagar, Maharashtra, India
Vaibhav S. Kanke
PDEA's Annasaheb Magar Mahavidyalaya
Rahul B. Bhakte
Dr. Babasaheb Ambedkar Marathwada University, Sub-Campus, Dharashiv (Chatrapati Sambhajinagar) 413 501, Maharashtra, India.
Amol R. Shelar
PDEA's Annasaheb Magar Mahavidyalaya
Prabhakar R. Kute
kuteprabhakar@gmail.com

Dr. Babasaheb Ambedkar Marathwada University

Research Article

Keywords: transition metal oxide, MgCo2O4, supercapacitor, green synthesis, Neem leaf extract, pseudocapacitor

Posted Date: November 23rd, 2026

DOI: https://doi.org/10.21203/rs.3.rs-11457551/v1

License: This work is licensed under a Creative Commons Attribution 4.0 International License.
Read Full License

Additional Declarations: No competing interests reported.

Neem-Mediated Morphology Evolution and Mg-Incorporated Cobalt Oxide Electrode Material for Supercapacitor Application.

Pankaj G. Patil[1], Vaibhav S. Kanke[2], Rahul B. Bhakte[3], Amol R. Shelar[4], Prabhakar R. Kute[1*]

[1]Deaprtment of Chemistry, Pratishthan Mahavidyalaya, Paithan 431107, Chatrapati Sambhajinagar, Maharashtra, India

[2]Department of Physics, PDEA's Annasaheb Magar Mahavidyalaya, Pune 411 028, Maharashtra, India

[3]Department of Chemistry, Dr. Babasaheb Ambedkar Marathwada University, Sub-Campus, Dharashiv (Chatrapati Sambhajinagar) 413 501, Maharashtra, India.

[4]Department of Chemistry, PDEA's Annasaheb Magar Mahavidyalaya, Hadapsar 411028, Pune, Maharashtra, India

Correspondence: Prabhakar R. Kute: kuteprabhakar@gmail.com

Abstract

In this study, a sol-gel auto-combustion route was employed to investigate the effects of fuel type and magnesium incorporation on the structural, morphological, surface, and electrochemical properties of cobalt-based oxides. Three electrodes were prepared: Co_3O_4 synthesized using citric acid (S1), Co_3O_4 prepared with neem leaf extract (S2), and $MgCo_2O_4$ synthesized using neem leaf extract (S3). XRD analysis confirmed the formation of the corresponding crystalline oxide phases. Concurrently, FE-SEM revealed a distinct morphological evolution from rock-like structures in citric-acid-derived Co_3O_4 to spherical features in neem-mediated Co_3O_4 and, subsequently, flake-like structures following magnesium incorporation. HR-TEM further confirmed the nanoscale morphology and crystalline nature of $MgCo_2O_4$. Among the synthesized electrodes, $MgCo_2O_4$ (S3) exhibited the highest specific capacitance, 991 F g^{-1} at 1 A g^{-1}, as well as an energy density of 31.73 Wh kg^{-1}, demonstrating its potential as a durable electrode material for high-performance supercapacitor applications.

Keywords: transition metal oxide, $MgCo_2O_4$, supercapacitor, green synthesis, Neem leaf extract, pseudocapacitor.

Introduction

The rapid growth of portable electronic devices, electric transportation, and renewable-energy technologies has created an increasing need for electrochemical energy-storage systems capable of providing high power, fast charge-discharge rates, and long-term operational stability. Among the various energy-storage technologies, supercapacitors have gained a distinctive position between conventional dielectric capacitors and batteries because of their rapid energy delivery and high-power capability and excellent cycling characteristics[1], [2]. Their electrochemical performance is closely related to the characteristics of the electrode material, including redox activity, electrical conductivity, accessible surface area, porosity, and the nature of the electrode-electrolyte interface. Therefore, designing electrode structures that enable efficient electron transport while maintaining rapid electrolyte-ion access remains an important focus of supercapacitor research [2], [3] . Transition metal oxides are particularly promising because their multiple oxidation states allow reversible faradaic reactions, offering higher charge-storage capability than conventional carbon-based electric double-layer electrodes. However, their practical application can be hindered by limited electrical conductivity, particle aggregation, sluggish ion diffusion, and structural degradation during repeated cycling. These challenges have encouraged increasing attention toward nanoscale structural design, compositional modification, and morphology engineering [2], [3], [4] .

Cobalt oxide is one of the widely investigated transition-metal oxides owing to its spinel structure, versatile cobalt redox chemistry, and ability to undergo reversible faradaic reactions. However, the electrochemical performance of cobalt oxide is highly dependent on its nanoscale structural arrangement. When the particles form dense aggregates, electrolyte penetration may become restricted, leaving part of the active material underutilized. In contrast, carefully designed nanoscale structures can provide greater exposure of electrochemically active interfaces and reduce the distance required for ion transport. Consequently, numerous cobalt oxide morphologies, such as porous, hollow, hierarchical, sheet-like, tubular, and particulate structures, have been explored for energy storage applications [2], [3]. Sol-gel auto-combustion offers several

advantages for oxide preparation because it allows intimate mixing of the precursor components before combustion, followed by rapid exothermic reaction which capable for the precursor components before combustion, followed by a rapid exothermic reaction capable of producing finely divided oxide.

Among plant-derived materials, neem (*Azadirachta indica*) is an interesting candidate for oxide synthesis because its extract contains various oxygen-containing organic constituents that can interact with metal precursors during material formation. Its role can extend beyond simply serving as an environmentally friendly substitute for a conventional reagent, since the chemically complex nature of the extract may affect nucleation and particle-growth processes and, consequently, the final architecture of the oxide [5], [6]. This aspect is particularly relevant for electrochemical electrodes because morphology directly influences electrolyte penetration, contact between the active material and electrolyte, and the participation of electrochemically generated species in subsequent reactions. Thus, the significance of the green approach lies not only in replacing a conventional reagent but also in producing demonstrable structural or morphological benefits [5], [6] .

$MgCo_2O_4$ is particularly promising in this context because magnesium cobaltite incorporates Mg and Co within a spinel-type cobaltite framework and has shown considerable potential as a supercapacitor electrode. Previous investigations have demonstrated appreciable charge-storage behavior influenced by the synthesis conditions and the resulting morphology. Different $MgCo_2O_4$ structures, including layered or flake-like, flower-like, spherical, and hierarchical architectures, have produced substantially different electrochemical responses, emphasizing the importance of controlling the physical arrangement of the active material [7], [8] . Recent reports have further indicated that morphology-engineered $MgCo_2O_4$ structures can improve electrolyte accessibility and electrochemical activity, highlighting the role of structural design in cobaltite-based electrodes [7], [8] .

Recent research further confirms that the electrochemical behavior of cobalt-based oxides is closely associated with synthesis strategy, morphology, and compositional modification. For instance, Ni et al. reported a dual-morphology $MgCo_2O_4$ composed of honeycomb-like and urchin-like structures directly grown on nickel foam. This interconnected architecture provides a specific

capacitance of 1552.34 F g^{-1} at 1 A g^{-1}, depicting the contribution of hierarchical structures to electrolyte accessibility and redox activity [9] . In another investigation, $MgCo_2O_4$ nanospheres prepared by the supercritical-CO_2-assisted solvothermal method exhibited an approximately 9 nm crystallite size and delivered a specific capacity of 449.3 C g^{-1} at 1 A g^{-1}. This result further illustrates the influence of synthesis conditions on crystallization and electrochemical performance [10] . A $MgCo_2O_4$/MgO microfiber system produced through a sol-gel route and reported in 2024 achieved a specific capacitance of 1091 F g^{-1} at 1 A g^{-1}, further demonstrating the suitability of sol-gel processing for producing electrochemically active cobalt-based structures [11]. More recently, Co_3O_4 anchored on g-C_3N_4 nanosheets delivered approximately 455 F g^{-1} at 1 A g^{-1} with 95 % of capacitance retention after 10,000 cycles, indicating the potential of two-dimensional supports to improve active-site accessibility and cycling stability [12] . Green synthesis has also been explored for modifying the morphology and surface characteristics of Co_3O_4. The synthesis of Co_3O_4 using *Calotropis procera* sap produced a heterogeneous nanoparticle and microclusters with reported capacitance of 700 F g-1 at 0.8 A g-1 [13]. In contrast, a 2025 study employing *Aloe vera* as a biogenic synthesis medium produced Co_3O_4 nanostructures with a specific capacitance of 467.9 F g^{-1} at 0.5 A g^{-1} and 83% capacitance retention after 3000 cycles [6] . Overall, these studies indicate that hierarchical morphology, green synthesis, heterostructure formation, and compositional modification can each contribute to improved electrochemical performance. However, these approaches have largely been examined separately.

A progressive comparison involving conventionally prepared Co_3O_4(S1), neem-mediated Co_3O_4 (S2), and finally neem-mediated $MgCo_2O_4$ (S3) allows these effects to be examined using a common sol-gel auto-combustion strategy. X-ray diffraction was employed to investigate phase formation and structural characteristics, while FE-SEM confirmed that the morphological evolution from pristine Co_3O_4 to $MgCo_2O_4$ is from rock-like to flake-like. The electrochemical behavior of the three electrodes was systematically assessed through cyclic voltammetry and galvanostatic charge-discharge; the electrochemical results, along with the observed structural and morphological changes, provide a synthesis-structure-performance relationship and highlight the potential of neem-mediated development.

2. Materials and method

2.1 Chemicals

Sigma-Aldrich Loba Chemicals supplied cobalt (II) nitrate hexahydrate ($Co(NO_3)_2 \cdot 6H_2O$; 99.99%), urea (NH_2CONH_2; 99.99%), magnesium nitrate hexahydrate ($Mg(NO_3)_2 \cdot 6H_2O$), citric acid, and ammonia solution (25%) as the starting reagents for the synthesis. Fresh neem (*Azadirachta indica*) leaves were used as a natural complexing/fuel source for the green synthesis. Distilled water was used throughout the experimental procedure. All chemicals were used as received without further purification.

2.2 Conventional synthesis of Co_3O_4 (S1)

Co_3O_4 was synthesized via a conventional sol-gel auto-combustion route using citric acid as the complexing and fuel agent. Initially, 7.25 g of cobalt nitrate hexahydrate was dissolved in 100 mL of distilled water under continuous magnetic stirring. Citric acid was subsequently added to the cobalt nitrate solution at a 1:1 molar ratio relative to the cobalt precursor. The resulting solution was stirred continuously for 1 h to ensure homogeneous mixing and effective complexation of the metal ions. Subsequently, a 25% ammonia solution was added dropwise under continuous stirring to adjust the pH of the precursor solution to approximately 7. The pH-adjusted solution was then heated under continuous stirring. As heating proceeded, the gradual evaporation of water led to the formation of a viscous gel. The resulting gel was transferred to a hot plate, where further heating promoted the self-propagating combustion of the organic component and the formation of a loose oxide precursor powder through the sol-gel auto-combustion process. The obtained powder was collected and manually ground using an agate mortar and pestle to produce a homogeneous precursor. Finally, the ground powder was calcined at 550 °C for 5 h to remove residual organic species and enhance the crystallinity of the oxide phase. The resulting Co_3O_4 powder was designated S1.

2.3 Green approach for synthesis of Co_3O_4

To replace the conventional citric-acid-based route, neem leaf extract was employed as a natural complexing and combustion-promoting agent. Approximately 10-20 fresh neem leaves were thoroughly washed with distilled water to remove surface impurities and subsequently boiled in distilled water for 2 h. After cooling, the solution was filtered to remove the leaf residues, and 10

mL of the resulting neem leaf extract was collected for use in the synthesis. For the preparation of Co_3O_4, 7.25 g of cobalt nitrate hexahydrate was dissolved in 100 mL of distilled water under continuous stirring. The prepared 10 mL neem leaf extract was then added to the cobalt precursor solution. The mixture was stirred for 1 h to facilitate interaction between the cobalt ions and the phytochemical constituents present in the extract. The pH was subsequently adjusted to approximately 7 using a 25% ammonia solution. The resulting solution was heated under continuous stirring until gel formation occurred. The viscous gel was then transferred to a hot plate, where further heating initiated auto-combustion, producing a voluminous precursor powder. The as-obtained powder was collected, thoroughly ground using a mortar and pestle, and calcined at 550 °C for 5 h. The resulting green-assisted Co_3O_4 powder was designated S2. An appropriate amount of magnesium nitrate hexahydrate was added to the aforementioned cobalt precursor while maintaining all other conditions unchanged. The resulting magnesium-incorporated cobalt oxide was designated S3.

2.4 Characterization techniques

The structural, morphological, surface, and electrochemical characteristics of the synthesized materials were systematically investigated using complementary characterization techniques. X-ray diffraction (XRD) was employed to identify the crystalline phases and examine the structural characteristics of the synthesized Co_3O_4 and $MgCo_2O_4$ materials. The diffraction patterns were analyzed to determine the characteristic crystallographic reflections and assess the phase formation and crystallinity of the samples. The surface morphology and particle architecture were examined using field-emission scanning electron microscopy (FE-SEM). The FE-SEM observations were used to establish the morphological evolution associated with the change from citric-acid-assisted synthesis to neem-mediated synthesis and subsequent Mg incorporation. High-resolution transmission electron microscopy (HR-TEM) was further employed for $MgCo_2O_4$ to investigate its nanoscale morphology, lattice fringes, crystallinity, and interplanar spacing.

2.4 Electrochemical techniques

The electrochemical behavior of all synthesized electrodes was evaluated using a three-electrode configuration in a 1 M KOH aqueous alkaline electrolyte. In this setup, Ag/AgCl served as the

counter electrode, platinum mesh as the reference electrode, and the synthesized S1, S2, and S3 materials as the working electrodes. Cyclic voltammetry (CV) was performed at scan rates ranging from 5 to 100 mV s^{-1} within a potential window of 0-0.5 V to examine the redox activity and charge-storage characteristics of the electrodes. Galvanostatic charge-discharge (GCD) measurements were conducted at current densities of 1, 2, 3, 4, 5, and 6 A g^{-1} to assess the specific capacitance, rate capability, and charge-discharge behavior within a potential window of 0-0.5 V. Electrochemical impedance spectroscopy (EIS) was carried out across a broad frequency range of 10 mHz to 100 kHz to investigate the interfacial charge-transfer characteristics, ionic and electronic transport behavior, and internal resistance of the electrodes. Long-term galvanostatic cycling was also performed to evaluate capacitance retention and electrochemical stability during repeated charge-discharge operation. Finally, the electrochemical results from the three samples were comparatively analyzed to clarify the relationships among synthesis strategy, morphology, composition, and charge-storage performance.

2.5 Electrode preparation

The nickel foam of thickness 0.5 mm was purchased from Vitra Technologies. A piece of 1*1.5 cm^2 of nickel foam was first sonicated in a 1 M HCl solution for the removal of the nickel oxide layer on the foam. Afterwards, the foam was sonicated in ethanol and distilled water, one after the other. Then it was dried at 70 ℃ for 3 hours. For preparation of the electrode slurry**,** 80 wt% of the synthesized active material, 10 wt% conductive carbon, and 10 wt% polyvinylidene fluoride (PVDF) binder were thoroughly mixed. N-methyl-2-pyrrolidone (NMP) was added gradually to the mixture to obtain a homogeneous and uniformly viscous slurry. The slurry was mechanically mixed until a consistent paste was obtained. The resulting slurry was then uniformly coated onto the pre-cleaned nickel foam using a spatula, ensuring good coverage of the conductive substrate. The coated electrodes were dried at 80 °C to remove the residual solvent and promote adhesion of the active material to the nickel foam.

3. Result and discussion

3.1 XRD analysis

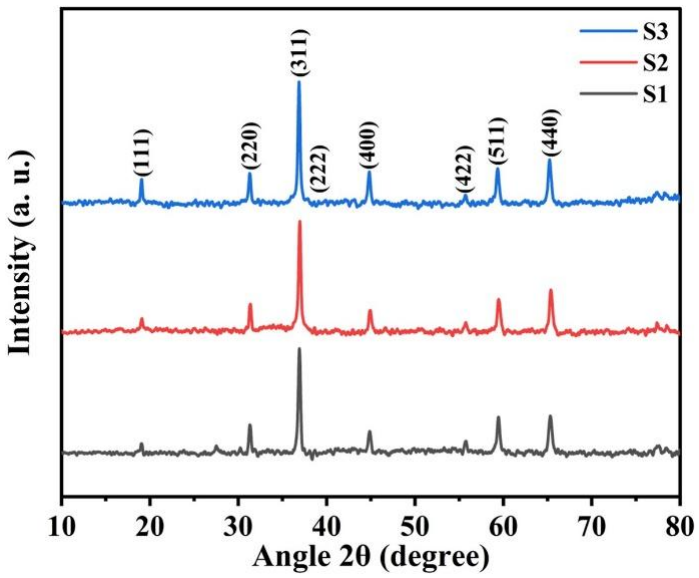

Fig. 1. X-Ray Diffraction plot of coded materials S1, S2, and S3.

The X-ray diffraction (XRD) patterns of the synthesized materials S1, S2, and S3 are presented in Fig. 1. The materials prepared using citric acid and neem leaf extract show distinct peaks at approximately 19°, 31°, 37°, 39°, 45°, 55°, 59°, and 65°, which can be indexed to the (111), (220), (311), (222), (400), (422), (511), and (440) planes, respectively. These reflections are characteristic of the cubic structure of cobalt oxide and match JCPDS Card No. 42-1467[14]. All of the characteristic reflections are observed for S2, in which neem leaf extract was used as the reducing and complexing agent. The main peaks remain at nearly the same positions, indicating that the plant extract does not alter the basic crystal structure of cobalt oxide [15] . Differences in the intensities of some diffraction peaks between S1 and S2 may be caused by variations in the combustion chemistry of citric acid and neem extract. The incorporation of Mg into cobalt oxide produces a diffraction pattern that retains the characteristic spinel reflections, with peaks assigned to the major crystallographic planes. This indicates that Mg is incorporated into the spinel oxide lattice without disrupting the overall cubic framework, leading to the formation of $MgCo_2O_4$. The absence of noticeable impurity reflections further supports the formation of the desired spinel phase[15] [16] . The crystallite size was calculated from these plots using the Scherrer equation.

$$D = \frac{K\,\lambda}{\beta\,Cos\,\theta} \qquad \text{(i)}$$

Where D is the mean size of the ordered crystalline domain (nm), K (=0.9) is the shape factor, λ represents the wavelength of Cu Kα X-ray radiation (0.15405 nm), β is the full width at half maximum (FWHM) of the diffraction peak in radians, and θ is the diffraction angle. The calculated crystallite sizes for materials S1, S2, and S3 are 20.39, 20.24, and 20.30 nm, respectively. No major change in crystallite size was observed among the materials. This minor variation may result from the change in the combustion agent from citric acid. This suggests that using neem leaf extract and incorporating Mg^{2+} has a limited effect on crystallite growth under the employed sol-gel autocombustion conditions. Overall, the XRD results confirm that both green synthesis using neem extract and Mg^{2+} incorporation preserve the spinel structure while modifying the structural characteristics of the resulting oxide [15], [17] .

3.2 FE-SEM analysis

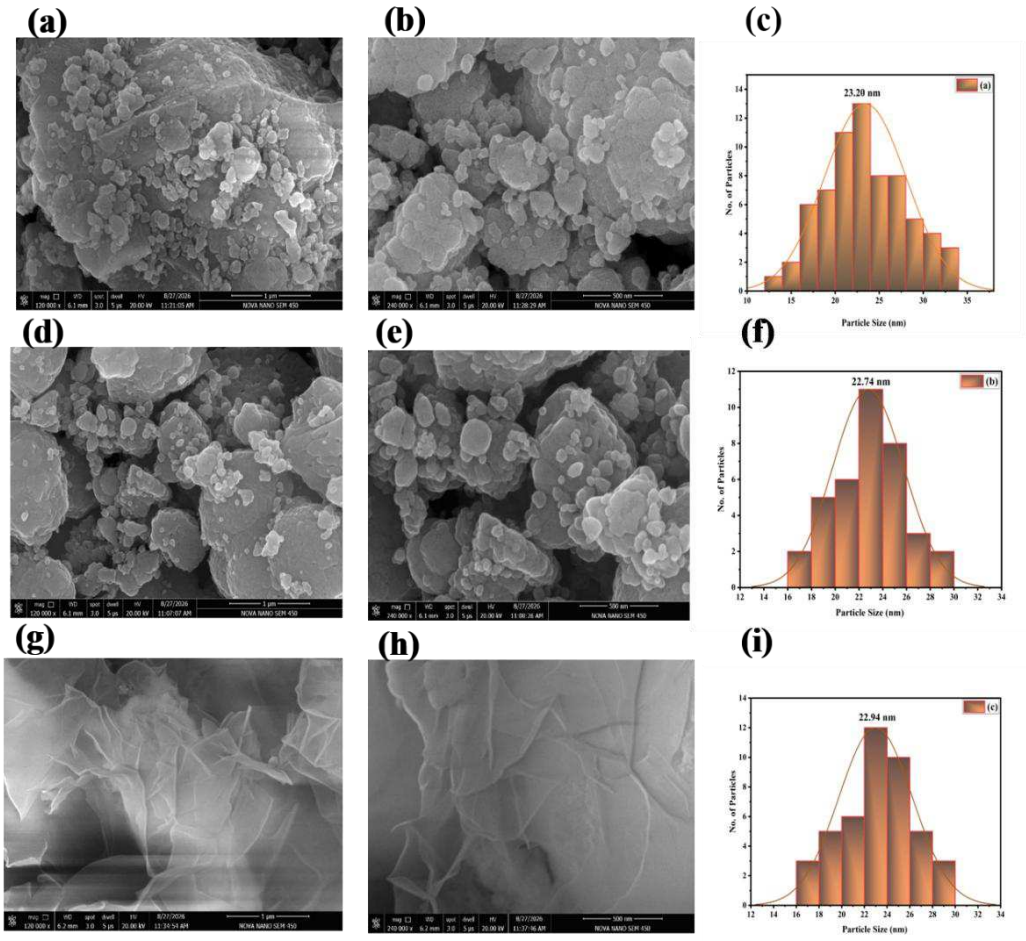

Fig. 2. FE-SEM images of synthesized nanomaterials. Fig (a-c) micrographs with histogram of sample S1, Fig (d-e) micrographs with histogram of sample S2, Fig (g-i) micrographs and histogram of sample S3

The surface morphology of the synthesized S1 and S2 Co_3O_4 nanoparticles was examined using field-emission scanning electron microscopy (FE-SEM). The FE-SEM images of S1, synthesized using citric acid, reveal predominantly irregular to nearly spherical nanoparticles with rough surfaces and evident agglomeration. This agglomeration is likely attributable to the high surface energy of nanoscale particles and strong interparticle interactions occurring during drying and subsequent thermal treatment. Higher-magnification images further reveal small nanoparticles dispersed across relatively large agglomerated regions. The average particle size is approximately 23.20 nm [5], [6] . In contrast, the S_2 Co_3O_4 nanoparticles synthesized using neem extract exhibit an irregular, rounded to quasi-spherical morphology with rough surfaces. The nanoparticles are present in a partially aggregated state, with numerous fine particles attached to larger particle clusters. Consequently, the S2 sample exhibits a slight decrease in average particle size, from 23.20 nm for S1 to 22.74 nm for S2, together with a comparatively narrower particle-size distribution [5], [15] .

The observed differences in morphology and particle-size distribution between S1 and S2 are attributable to the distinct chemical environments created by citric acid and neem extract during nanoparticle formation. Citric acid primarily functions as a complexing agent, coordinating with cobalt ions and promoting the homogeneous formation of precursors throughout the synthesis process. In contrast, neem extract contains a range of naturally occurring phytochemicals, including polyphenolic, flavonoid, terpenoid, protein, and other oxygen-containing functional groups, which can interact with cobalt precursor species and newly formed Co_3O_4 nuclei. These phytochemicals can exert complexing, stabilizing, and capping effects, thereby modulating nucleation and limiting excessive particle growth. Consequently, neem-mediated synthesis may favor the formation of relatively finer and more uniformly distributed nanoparticles, as observed for S2. The slightly smaller average particle size of S2 relative to S1 indicates that neem-derived phytochemicals exert a measurable influence on particle-growth control. The narrower distribution observed for S2 also suggests more effective stabilization of the growing nanoparticles during synthesis. Nevertheless, the presence of agglomeration in both samples indicates that the high

surface energy of the nanoparticles continues to promote particle-particle interactions during drying and thermal treatment. The nanoscale dimensions and rough surface morphologies of both samples indicate a potentially large exposed surface area [18], [19], [20] . FE-SEM micrographs of the synthesized S3 $MgCo_2O_4$ nanoparticles prepared using neem extract reveal a distinctive wrinkled, flake-like, and sheet-type morphology, consisting of relatively extended structures with irregular edges and interconnected regions. The higher-magnification micrograph clearly demonstrates the folded and layered nature of these structures, with numerous nanoscale features distributed across their surfaces. In contrast to the relatively irregular to quasi-spherical morphology observed for the Co_3O_4 samples, S3 exhibits a more pronounced sheet-like architecture, indicating that the nature of the metal precursors and the interaction of the mixed-metal system with neem extract influence the morphology during synthesis. The formation of this characteristic morphology may be associated with the presence of neem-derived phytochemicals, which can interact with Mg^{2+} and Co^{2+} precursor ions and subsequently with the newly formed oxide nuclei. The various organic constituents of neem extract, particularly oxygen-containing functional groups, can act as complexing, stabilizing, and capping species, thereby modifying the nucleation rate and subsequent growth of $MgCo_2O_4$. These interactions may promote controlled nucleation and the preferential growth of nanoscale oxide features [7], [18]. The particle-size distribution obtained from the FE-SEM micrographs indicates that the measured nanoscale features are primarily distributed around an average particle size of approximately 22.94 nm, confirming the nanoscale nature of the synthesized $MgCo_2O_4$ material. These characteristics of the green synthesis approach may further influence the electrochemical properties of the material, as reflected in its electrochemical response and the enhanced incorporation of Mg [7], [21] .

3.3 HR-TEM analysis

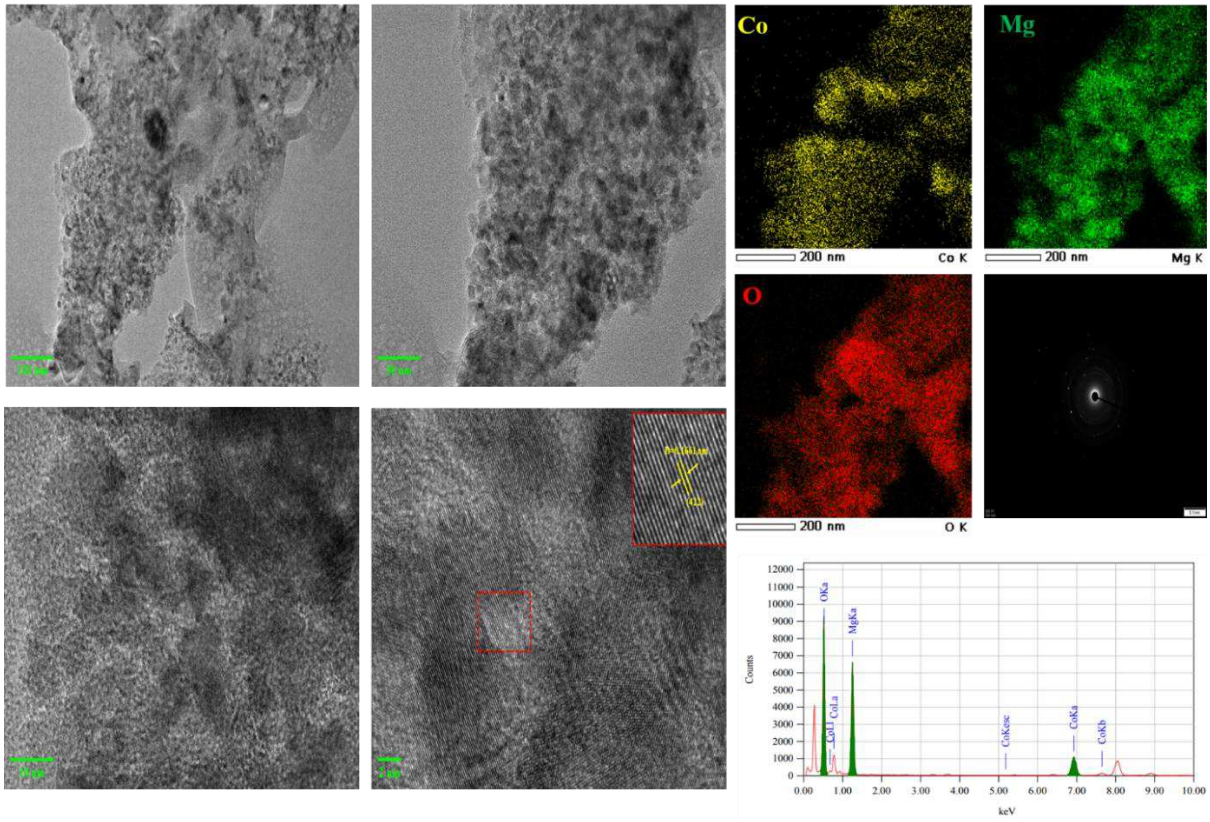

Fig. 3. High-resolution transmission electron microscopy (HR-TEM) graph of material S3, crystallite size, elemental mapping, SAED pattern.

HR-TEM analysis offers additional insight into the nanoscale structure and crystallinity of the neem-assisted $MgCo_2O_4$ sample. At low and intermediate magnifications, the HR-TEM images show irregular, flake-like assemblies made up of densely interconnected nanoscale domains, with clear interparticle contrast and visible void spaces. This morphology agrees well with the flake-like architecture observed by FE-SEM and points to a highly divided structure with numerous exposed interfaces. Such an architecture can improve electrolyte accessibility and shorten ion-transport distances, potentially contributing to the electrochemical response of the $MgCo_2O_4$ electrode [9], [22] .

At higher magnification, well-defined and continuous lattice fringes are visible, confirming the crystalline nature of the material. The measured interplanar spacing of approximately 0.161 nm matches the (422) plane of cubic spinel $MgCo_2O_4$, supporting the formation of the spinel phase identified by XRD (fig. 1). The corresponding FFT pattern shows concentric diffraction rings, indicating multiple randomly oriented nanocrystalline domains within the examined region. These

HR-TEM observations therefore complement the XRD results by offering direct, real-space evidence of crystalline ordering at the nanoscale [9], [22], [23] .

The STEM-EDS elemental maps show a broadly homogeneous distribution of Mg, Co, and O throughout the analyzed region, indicating that the constituent elements are closely co-distributed within the flake-like structure. The corresponding EDS spectrum further confirms the presence of Mg, Co, and O, supporting the formation of the mixed-metal oxide. Overall, the combined evidence from the nanoscale flake-like morphology, clearly resolved spinel lattice fringes, FFT diffraction features, and homogeneous elemental distribution provides strong microscopic support for the successful formation of crystalline $MgCo_2O_4$. The structural features developed through the neem-assisted synthesis may promote surface accessibility and interconnected transport pathways for electrochemical charge storage. The interconnected nanoscale crystalline domains and open flake-like architecture create abundant accessible interfaces for electrolyte interaction, while the short diffusion lengths can support rapid ion transport during electrochemical cycling. This structural configuration is therefore well suited to the efficient utilization of redox-active sites and may contribute to the enhanced charge-storage performance and rate response of the $MgCo_2O_4$ electrode [16], [22], [24] .

3.4 Electrochemical analysis

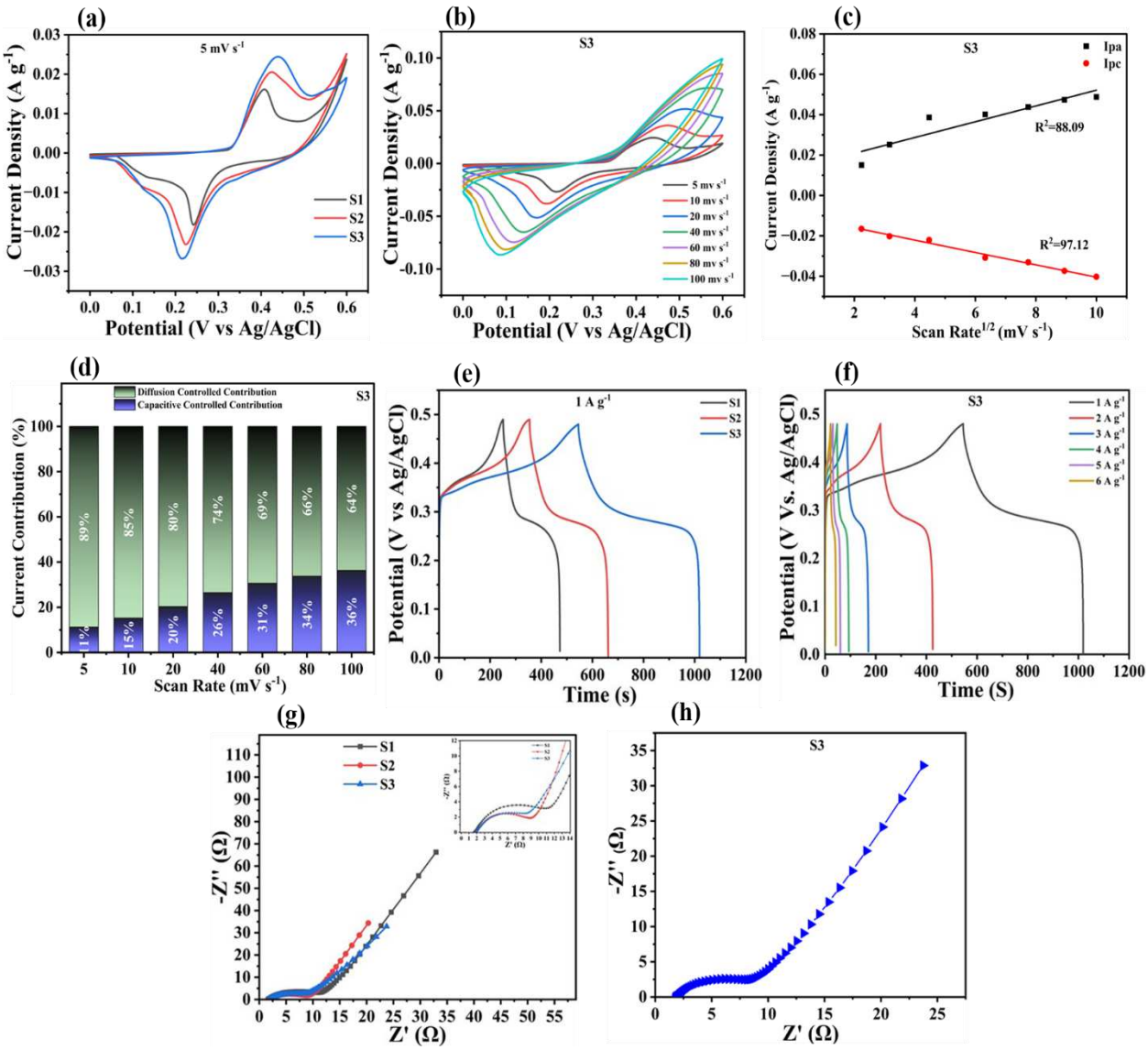

Fig. 4 (a) Comparative Cyclic voltammogram of all three materials (S1, S2, and S3) at a scan rate of 5 mV s-1, (b) cyclic voltammetry of material S3, ranging from 5- 100 mV s-1, (c) graph of peak current vs. scan rate. (d) distribution of capacitive and diffusion-controlled contributions with scan rate ranging from 5- 100 mV s-1, (e) comparative GCD curve of material S1, S2, and S3 at a current density of 1 A g^{-1}, (f) GCD curves of material S3, ranging from 1-6 A g^{-1}, (g) comparative EIS of material S1, S2, and S3. (h) EIS of material S3

The electrochemical behavior of S1 (Co_3O_4-citric acid), S2 (Co_3O_4-neem extract), and S3 ($MgCo_2O_4$-neem extract) was investigated using a three-electrode configuration. The cyclic

voltammetry (CV) curves recorded at 5 mV s^{-1} (Fig. 4a) exhibit distinct redox features, confirming that charge storage is primarily associated with reversible faradaic reactions, accompanied by a surface-controlled capacitive contribution [22], [25]. Among the three electrodes, S3 exhibits the largest integrated CV area and the highest redox current, indicating superior electrochemically accessible charge-storage capacity. The enhancement observed from S1 to S2 suggests that neem-assisted synthesis modifies the surface architecture and improves the accessibility of Co_3O_4. The further increase observed for S3 indicates an additional contribution from Mg incorporation. Because no substantial variation in crystallite size was observed by XRD, the enhanced electrochemical response is more reasonably attributed to differences in surface morphology, active-site accessibility, and electrode-electrolyte interaction [16], [23] .

The scan-rate-dependent CV curves of S3 (Fig. 4. b) maintain their characteristic redox features across scan rates from 5 to 100 mV s^{-1}. Although the peak positions gradually shift as the scan rate increases, this behavior suggests greater polarization and finite ion-transport limitations at higher rates [25], [26] . The relationship between peak current and the square root of the scan rate (Fig. 4. c) shows an approximately linear trend, with R^2 values of 0.8809 and 0.9712 for the anodic and cathodic processes, respectively. These results confirm that diffusion makes a significant contribution to the faradaic charge-storage process. At the same time, the deviation from ideal linearity indicates that the overall response is not governed exclusively by diffusion. The charge-storage kinetics were further quantified using the relation

$$i = k_1 v + k_2 v^{1/2} \quad (ii)$$

$$1\ \frac{i}{v^{1/2}} = k_1 v + k_2 \quad (iii)$$

The constants k_1 and k_2, representing surface- and diffusion-controlled contributions, respectively, were determined from the i vs. v^1/2 and i/v^1/2 vs. v^1/2 plots. As shown in (Fig. 4. d), the diffusion-controlled contribution decreases from 89% at 5 mV s^{-1} to 64% at 100 mV s^{-1}, whereas the capacitive contribution increases from 11% to 36%. At low scan rates, sufficient time is available for electrolyte ions to penetrate more deeply into the electrode and participate in faradaic reactions, resulting in predominantly diffusion-controlled charge storage. As the scan rate increases, ion diffusion becomes progressively restricted, and rapidly accessible surface and near-surface sites contribute increasingly to the total current [26], [27] . Thus, S3 exhibits a mixed

charge-storage mechanism in which diffusion-assisted faradaic reactions dominate at low scan rates, whereas surface-controlled processes become increasingly significant at high scan rates [27] . The GCD profiles recorded at 1 A g^{-1} (Fig. 4. e) further demonstrate the superior charge-storage capability of S3. The discharge time increases systematically from S1 to S3, consistent with the larger CV area observed for S3. The specific capacitance, energy density, and power density were calculated using the following equations:

$$Specific\ capacitance\ (C)(F/g) = \frac{I\ (mA) \times t_d(s)}{m\ (mg) \times \Delta V\ (V)} \quad \text{(iv)}$$

Where I is current (mA), t_d is discharge time (s), m is active mass of material (mg), and ΔV is potential window (V) in which GCD is performed.

$$Energy\ Density\ \left(E_g\right)\ \left(\frac{Wh}{Kg}\right) = \frac{C\ (F/g) \times \Delta V^2\ (V)}{2 \times 3.6} \quad \text{(vi)}$$

$$Power\ Density\ \left(P_g\right)\ \left(\frac{W}{Kg}\right) = \frac{E_g\ (Wh/Kg) \times 3600}{3600} \quad \text{(vii)}$$

The calculated specific capacitances are approximately 460 F g^{-1}, 644 F g^{-1}, and 992 F g^{-1} for S1, S2, and S3, respectively, at 1 A g^{-1}. The notably higher capacitance of S3 highlights the more effective utilization of its electrochemically active sites following Mg incorporation and the formation of a flake-like morphology. The GCD profiles of S3 at increasing current densities (Fig. 4. f) show the expected decrease in discharge time as the current increases, while maintaining their characteristic nonlinear faradaic profiles. Retention of the overall profile at higher current densities indicates that a considerable fraction of the accessible active sites remains electrochemically available under accelerated charge-discharge conditions [25], [27] . This observation is consistent with the increasing capacitive contribution identified through kinetic analysis and suggests that readily accessible surface and near-surface sites help offset, to some extent, the reduced ion-diffusion time at high rates [26], [28]. The Nyquist plots (Fig. 4. g,h) provide complementary information regarding the interfacial charge-transfer and ion-transport characteristics. Equivalent-circuit fitting yields the circuit Rs-(Rct‖CPE)-W. The high-frequency intercept corresponds to the equivalent series resistance (Rs), whereas the depressed semicircle is associated with the charge-transfer resistance (Rct) and nonideal interfacial capacitive behavior. The inclined region at low

frequencies represents ion diffusion and the capacitive response within the porous electrode [9], [29] . S3 exhibits a comparatively favorable impedance response, indicating efficient interfacial charge transfer and electrolyte interaction.

Table 1. Comparison of other study of Mg-incorporated morphology-oriented synthesis.

Sr. No	**Materials**	**Electrolyte**	**Synthesis route**	**Specific Capacitance**	**Reference**
1	$MgCo_2O_4$	3 M LiOH	Molten-salt method	~320 F g^{-1}	[30]
2	$MgCo_2O_4$ (oxygen-vacancy-free)	1M KOH	Hydrothermal synthesis	340 F g^{-1} at 1 A g^{-1}	[24]
3	$MgCo_2O_4$ nanofibres	2M KOH	Sol-gel electrospinning	210 F g^{-1} at 0.5 A g^{-1}	[31]
4	$MgCo_2O_4$ microflowers	2 M KOH	Hydrothermal followed by calcination	749.2 F g^{-1} at 1 A g^{-1}	[32]
5	Double-urchin-like $MgCo_2O_4$	3 M KOH	Hydrothermal	508 F g^{-1} at 2 A g^{-1}	[33]
6	$MgCo_2O_4$ porous nanoflakes	6 M KOH	Hydrothermal followed by calcination	734.1 F g^{-1} at 1 A g^{-1}	[22]
7	$MgCo_2O_4$ twinned hemispheres	1 M KOH	Solvothermal	626.5 F g^{-1} at 1 A g^{-1}	[34]
8	$MgCo_2O_4$ nanocone arrays on Ni foam	1 M Na_2SO_4	One-step hydrothermal	750 F g^{-1} at 1 A g^{-1}	[35]

9	$MgCo_2O_4$ microflowers	2 M KOH	Hydrothermal	696.2 F g^{-1} at 1 A g^{-1}	[16]
10	$MgCo_2O_4$ (CTAB-templated)	1 M KOH	CTAB-assisted hydrothermal	711 F g^{-1} at 1 A g^{-1}	[36]
11	$MgCo_2O_4$	1 M KOH	Sol-gel Green synthesis	991 F g^{-1} at 1 A g^{-1}	This work

4. Conclusion

In this study, the morphological evolution and enhancement in pseudocapacitive behavior were successfully achieved via the sol-gel auto-combustion technique. A green approach was also introduced with further Mg incorporation in cobalt oxide. The crystallinity and phase purity were depicted by XRD plots; the absence of any impurity peak reflects the purity. The material S1 with citric acid, S2 with neem-leaf extract, and S3 with further Mg incorporation give crystallite sizes of 20.39, 20.30, and 20.24 nm, respectively. The crystallinity and plane formation were again confirmed by HR-TEM study. The presence of elemental mapping inside the material of sample S3 also confirmed with elemental mapping. The morphological evolution of the material with a stepwise additive approach was confirmed by FE-SEM images. The average particle size achieved was depicted with the help of a histograms. The electrochemical study of all three materials was done, and material S3 shows the highest capacitance of 991 F g^{-1} at a current density of 1 A g^{-1} and shows energy density and power density of 31.73 Wh kg^{-1} and 240 W kg^{-1}, which shows an enhancement nearly twice that of pristine cobalt oxide.

CRediT authorship contribution statement

Pankaj G. Patil: Investigation, Methodology, Formal analysis, Writing - original draft. **Vaibhav S. Kanke:** Investigation, Validation. **Rahul B. Bhakte:** Data curation. **Amol R. Shelar:** Resources, Investigation. **Dr. Prabhakar R. Kute:** Conceptualization, Supervision, Project administration, Writing - review & editing.

Declaration of competing interest

The authors declare that they have no known competing financial interests or personal relationships that could have appeared to influence the work reported in this paper.

Data availability

Data will be made available on request.

Funding

This research did not receive any specific grant from funding agencies in the public, commercial, or not-for-profit sectors.

Acknowledgements

One of the author Pankaj G. Patil thanks to their respective institutions for providing laboratory facilities, and acknowledge the assistance of the characterisation facility at Deaprtment of Chemistry, Pratishthan Mahavidyalaya, Paithan, Chatrapati Sambhajinagar, Maharashtra, India .

References

[1] P. Simon and Y. Gogotsi, “Materials for electrochemical capacitors,” *Nature Materials 2008 7:11*, vol. 7, no. 11, pp. 845-854, Nov. 2008, doi: 10.1038/nmat2297.

[2] R. Liang *et al.*, “Transition Metal Oxide Electrode Materials for Supercapacitors: A Review of Recent Developments,” *Nanomaterials 2021, Vol. 11, Page 1248*, vol. 11, no. 5, p. 1248, May 2021, doi: 10.3390/NANO11051248.

[3] P. Gaikwad, N. Tiwari, R. Kamat, S. M. Mane, and S. B. Kulkarni, “A comprehensive review on the progress of transition metal oxides materials as a supercapacitor electrode,” *Materials Science and Engineering: B*, vol. 307, p. 117544, Sep. 2024, doi: 10.1016/J.MSEB.2024.117544.

[4] X. Zhu, “Recent advances of transition metal oxides and chalcogenides in pseudo-capacitors and hybrid capacitors: A review of structures, synthetic strategies, and mechanism studies,” *J. Energy Storage*, vol. 49, p. 104148, May 2022, doi: 10.1016/J.EST.2022.104148.

[5] A. L. Bhatti *et al.*, “Facile synthesis of efficient Co3O4 nanostructures using the milky sap of Calotropis procera for oxygen evolution reactions and supercapacitor applications,” *RSC Adv.*, vol. 13, no. 26, pp. 17710-17726, Jun. 2023, doi: 10.1039/D3RA02555A.

[6] M. Bhatt, K. Gautam, P. Dhyani, and A. K. Sinha, “Green synthesis of Aloe vera-assisted Co3O4 nanostructures: structural, electronic, optical, and electrochemical insights for supercapattery applications,” *RSC Adv.*, vol. 15, no. 35, pp. 28626-28641, Aug. 2025, doi: 10.1039/D5RA03604F.

[7] J. Bhagwan and J. I. Han, “High-performance asymmetric supercapacitor of sol-gel routed MgCo2O4/MgO microfiber,” *J. Energy Storage*, vol. 94, p. 112463, Jul. 2024, doi: 10.1016/J.EST.2024.112463.

[8] Z. Liu, Q. Xiang, H. Zhang, X. Zhang, H. Tan, and Y. Zhao, “Supercritical CO2-assisted solvothermal synthesis and characterization of MgCo2O4 nanospheres for high-performance capacitance,” *Ceram. Int.*, vol. 50, no. 5, pp. 7789-7797, Mar. 2024, doi: 10.1016/J.CERAMINT.2023.12.105.

[9] H. Ni *et al.*, “Facile synthesis of dual-morphological MgCo2O4 with remarkable performance for pseudosupercapacitors,” *Mater. Adv.*, vol. 4, no. 1, pp. 134-149, Jan. 2023, doi: 10.1039/D2MA00889K.

[10] Z. Liu, Q. Xiang, H. Zhang, X. Zhang, H. Tan, and Y. Zhao, “Supercritical CO2-assisted solvothermal synthesis and characterization of MgCo2O4 nanospheres for high-performance capacitance,” *Ceram. Int.*, vol. 50, no. 5, pp. 7789-7797, Mar. 2024, doi: 10.1016/J.CERAMINT.2023.12.105.

[11] J. Bhagwan and J. I. Han, “High-performance asymmetric supercapacitor of sol-gel routed MgCo2O4/MgO microfiber,” *J. Energy Storage*, vol. 94, p. 112463, Jul. 2024, doi: 10.1016/J.EST.2024.112463.

[12] M. Subbiah, A. Radhakrishnan, M. Tharmaraj, A. Lakshmanan, S. Venkatachalam, and N. Srinivasan, “Facile synthesis of mesoporous Co3O4 anchoring on the g-C3N4 nanosheets for high performance supercapacitor,” *J. Alloys Compd.*, vol. 1008, p. 176689, Dec. 2024, doi: 10.1016/J.JALLCOM.2024.176689.

[13] A. L. Bhatti *et al.*, “Facile synthesis of efficient Co3O4 nanostructures using the milky sap of Calotropis procera for oxygen evolution reactions and supercapacitor applications,” *RSC Adv.*, vol. 13, no. 26, pp. 17710-17726, Jun. 2023, doi: 10.1039/D3RA02555A.

[14] A. Umar *et al.*, “Perforated Co3O4 nanosheets as high-performing supercapacitor material,” *Electrochim. Acta*, vol. 389, p. 138661, Sep. 2021, doi: 10.1016/J.ELECTACTA.2021.138661.

[15] C. T. Anuradha and P. Raji, “Facile-synthesis and characterization of cobalt oxide (Co3O4) nanoparticles by using Arishta leaves assisted biological molecules and its antibacterial and antifungal activities,” *J. Mol. Struct.*, vol. 1262, p. 133065, Aug. 2022, doi: 10.1016/J.MOLSTRUC.2022.133065.

[16] H. Ni *et al.*, “Facile synthesis of dual-morphological MgCo2O4 with remarkable performance for pseudosupercapacitors,” *Mater. Adv.*, vol. 4, no. 1, pp. 134-149, Jan. 2023, doi: 10.1039/D2MA00889K.

[17] P. Kulkarni, D. Ghosh, G. Balakrishna, R. S. Rawat, M. V. Reddy, and S. Adams, “Facile high yield synthesis of MgCo2O4 and investigation of its role as anode material for lithium ion batteries,” *Ceram. Int.*, vol. 45, no. 12, pp. 14775-14782, Aug. 2019, doi: 10.1016/J.CERAMINT.2019.04.205.

[18] F. Mwangi, J. Zia, and U. Riaz, “Green Synthesis of Metal Oxide Nanoparticles Using Plant Extracts: Applications in Catalysis and Biomedicine,” *Nano Select*, vol. 7, no. 3, p. e70117, Mar. 2026, doi: 10.1002/NANO.70117.

[19] N. Annu, M. Sahu, S. Singh, S. Prajapati, D. K. Verma, and D. K. Shin, “From green chemistry to biomedicine: the sustainable symphony of cobalt oxide nanoparticles,” *RSC Adv.*, vol. 14, no. 45, pp. 32733-32758, Oct. 2024, doi: 10.1039/D4RA05872K.

[20] S. N. Tanwar, Y. R. Parauha, Y. There, H. C. Swart, and S. J. Dhoble, “Plant-Based Biosynthesis of Metal and Metal Oxide Nanoparticles: An Update on Antimicrobial and Anticancer Activity,” *ChemBioEng Reviews*, vol. 11, no. 6, p. e202400012, Dec. 2024, doi: 10.1002/CBEN.202400012;CTYPE:STRING:JOURNAL.

[21] I. J. Lithi, K. I. Ahmed Nakib, A. M. S. Chowdhury, and M. Sahadat Hossain, “A review on the green synthesis of metal (Ag, Cu, and Au) and metal oxide (ZnO, MgO, Co3O4, and TiO2) nanoparticles using plant extracts for developing antimicrobial properties,” *Nanoscale Adv.*, vol. 7, no. 9, pp. 2446-2473, Apr. 2025, doi: 10.1039/D5NA00037H.

[22] H. Chen *et al.*, “Facile hydrothermal synthesis of porous MgCo2O4 nanoflakes as an electrode material for high-performance asymmetric supercapacitors,” *Nanoscale Adv.*, vol. 2, no. 8, pp. 3263-3275, Aug. 2020, doi: 10.1039/D0NA00353K.

[23] H. M. Arbi *et al.*, “Hierarchically Developed Ni(OH)2@MgCo2O4 Nanosheet Composites for Boosting Supercapacitor Performance,” *Nanomaterials*, vol. 13, no. 8, p. 1414, Apr. 2023, doi: 10.3390/NANO13081414/S1.

[24] H. Wang, N. Mi, S. Sun, W. Zhang, and S. Yao, “Oxygen vacancies enhancing capacitance of MgCo2O4 for high performance asymmetric supercapacitors,” *J. Alloys Compd.*, vol. 869, p. 159294, Jul. 2021, doi: 10.1016/J.JALLCOM.2021.159294.

[25] S. Vijayakumar, S. Nagamuthu, and K. S. Ryu, “In situ preparation of MgCo2O4 nanosheets on Ni-foam as a binder-free electrode for high performance hybrid supercapacitors,” *Dalton Transactions*, vol. 47, no. 19, pp. 6722-6728, May 2018, doi: 10.1039/C8DT00591E.

[26] S. Sharma and P. Chand, “Supercapacitor and electrochemical techniques: A brief review,” *Results Chem.*, vol. 5, p. 100885, Jan. 2023, doi: 10.1016/J.RECHEM.2023.100885.

[27] C. Liu, F. Li, M. Lai-Peng, and H. M. Cheng, “Advanced materials for energy storage,” *Advanced Materials*, vol. 22, no. 8, Feb. 2010, doi: 10.1002/ADMA.200903328.

[28] P. Rawat, M. H. Lee, A. Kumar, S. Thoravat, and J. S. Rhyee, “Thermoelectric properties of extrinsic phase mixing in chalcogenide bulk nanocomposites,” *Current Applied Physics*, vol. 60, pp. 15-31, Apr. 2024, doi: 10.1016/J.CAP.2024.01.007.

[29] X. Wang *et al.*, “Preparation and Electrochemical Properties of Co3O4 Supercapacitor Electrode Materials,” *Crystals 2020, Vol. 10, Page 720*, vol. 10, no. 9, p. 720, Aug. 2020, doi: 10.3390/CRYST10090720.

[30] S. G. Krishnan *et al.*, “Characterization of MgCo2O4 as an electrode for high performance supercapacitors,” *Electrochim. Acta*, vol. 161, pp. 312-321, Apr. 2015, doi: 10.1016/J.ELECTACTA.2015.02.081.

[31] M. M. Ghaziani, J. Mazloom, and F. E. Ghodsi, “Electrospun MgCo2O4 nanofibers as an efficient electrode material for pseudocapacitor applications: Effect of calcination temperature on electrochemical performance,” *Journal of Physics and Chemistry of Solids*, vol. 152, p. 109981, May 2021, doi: 10.1016/J.JPCS.2021.109981.

[32] Y. Wang, J. Sun, S. Li, Y. Zhang, C. Xu, and H. Chen, “Hydrothermal synthesis of flower-like MgCo2O4 porous microstructures as high-performance electrode material for asymmetric supercapacitors,” *J. Alloys Compd.*, vol. 824, p. 153939, May 2020, doi: 10.1016/J.JALLCOM.2020.153939.

[33] J. Xu *et al.*, “Fabrication of porous double-urchin-like MgCo2O4 hierarchical architectures for high-rate supercapacitors,” *J. Alloys Compd.*, vol. 688, pp. 933-938, Dec. 2016, doi: 10.1016/J.JALLCOM.2016.07.250.

[34] Y. Wang *et al.*, “Facile solvothermal synthesis of novel MgCo2O4 twinned-hemispheres for high performance asymmetric supercapacitors,” *J. Alloys Compd.*, vol. 818, p. 152905, Mar. 2020, doi: 10.1016/J.JALLCOM.2019.152905.

[35] L. Cui *et al.*, “High-performance MgCo2O4 nanocone arrays grown on three-dimensional nickel foams: Preparation and application as binder-free electrode for pseudo-supercapacitor,” *J. Power Sources*, vol. 333, pp. 118-124, Nov. 2016, doi: 10.1016/J.JPOWSOUR.2016.09.159.

[36] T. A. Sandosh and A. Simi, “Facile and Cost-Effective CTAB Templated Hydrothermal Synthesis and Characterization of MgCo2O4 Electrode Material for Supercapacitor Application,” *J. Inorg. Organomet. Polym. Mater.*, vol. 31, no. 1, pp. 251-260, Jan. 2021, doi: 10.1007/S10904-020-01671-X/FIGURES/9.